# Spatially Resolved Mapping of Electrical Conductivity across Individual Domain (Grain) Boundaries in Graphene

**Kendal W. Clark,[†] X.-G. Zhang,[†] Ivan V. Vlassiouk,[‡] Guowei He,[§] Randall M. Feenstra,[§] and An-Ping Li[†,*]**

[†]Center for Nanophase Materials Sciences, Oak Ridge National Laboratory, Oak Ridge, Tennessee 37831, United States, [‡]Measurement Science & Systems Engineering Division, Oak Ridge National Laboratory, Oak Ridge, Tennessee 37831, United States, and [§]Department of Physics, Carnegie Mellon University, Pittsburgh, Pennsylvania 15213, United States

**ABSTRACT** All large-scale graphene films contain extended topological defects dividing graphene into domains or grains. Here, we spatially map electronic transport near specific domain and grain boundaries in both epitaxial graphene grown on SiC and CVD graphene on Cu subsequently transferred to a $SiO_2$ substrate, with one-to-one correspondence to boundary structures. Boundaries coinciding with the substrate step on SiC exhibit a significant potential barrier for electron transport of epitaxial graphene due to the reduced charge transfer from the substrate near the step edge. Moreover, monolayer–bilayer boundaries exhibit a high resistance that can change depending on the height of substrate step coinciding at the boundary. In CVD graphene, the resistance of a grain boundary changes with the width of the disordered transition region between adjacent grains. A quantitative modeling of boundary resistance reveals the increased electron Fermi wave vector within the boundary region, possibly due to boundary induced charge density variation. Understanding how resistance change with domain (grain) boundary structure in graphene is a crucial first step for controlled engineering of defects in large-scale graphene films.

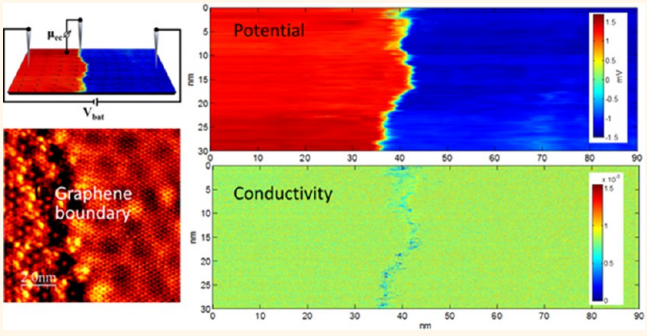


**KEYWORDS:** graphene · electronic transport · grain boundary · defect · scanning tunneling microscopy · potentiometry

Graphene, because of its unique electronic structure, has quickly become one of the most notable "wonder-materials" poised to transform the electronics and nanotechnology landscape.[1] The proposed applications could push the existing limits of microelectronics, chemical sensing instruments, biosensors, ultracapacitance devices, flexible displays and other innovations. Targeting such applications, researchers are investigating large-scale graphene synthesis by thermal decomposition of Si from SiC (0001) surfaces[2] as well as chemical vapor deposition (CVD) on noble and transition metal substrates.[3] The symmetry of the graphene honeycomb lattice is a key factor in determining many of graphene's unique electronic properties and application prospects.[4] However, all large-scale graphene contain structural defects. The high density of substrate steps[5,6] and changes in graphene layer thickness[7–9] can seriously degrade electron transport properties in epitaxial graphene films on SiC. CVD growth of graphene on Cu is able to produce predominantly monolayer graphene.[3] But large-scale graphene is often polycrystalline consisting of randomly oriented domains.[10–17] Domain shapes depend on growth conditions yielding hexagonal grains in our APCVD approach. When these individual graphene grains coalesce into a film, graphene grain boundaries (GBs) form. These extended defects break the lattice symmetry and are believed to have a major impact on the electronic properties, especially in transport, along the graphene sheets.[14,18,19] Huang *et al.* detected no measurable electrical resistance from GBs within their instrument limit.[20] However, Yu *et al.*

* Address correspondence to apli@ornl.gov.

Received for review June 17, 2013 and accepted August 16, 2013.

**Published online** 10.1021/nn403056k

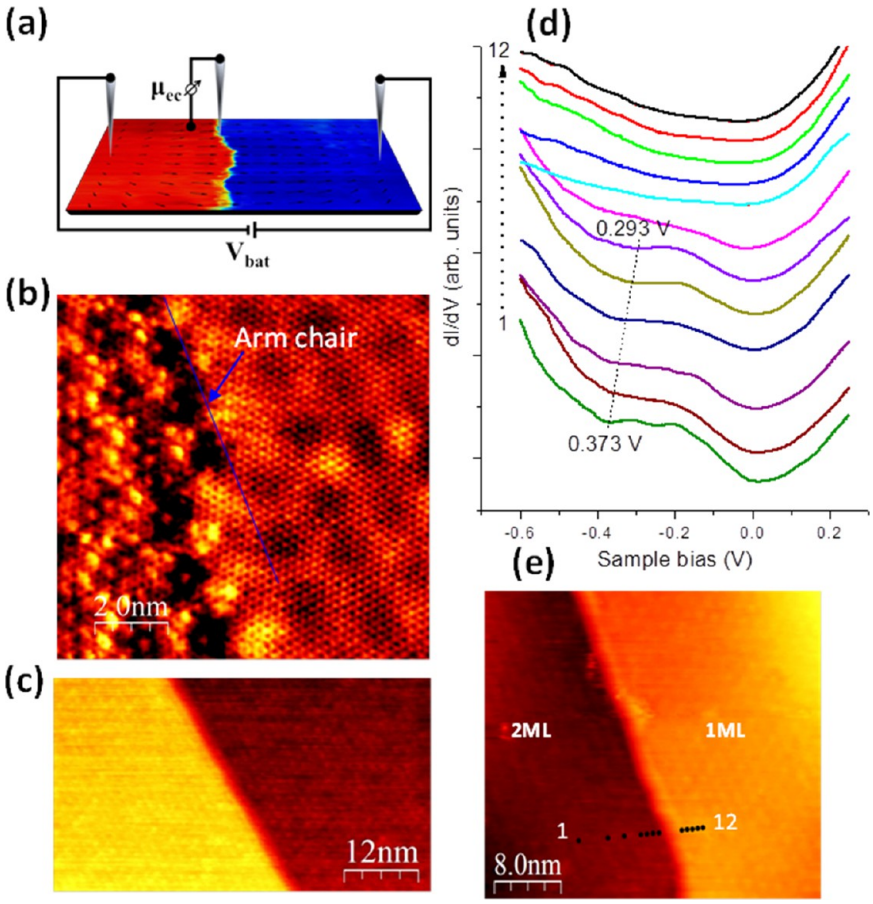


**Figure 1. Characterization of epitaxial graphene on a SiC substrate. (a) Schematic of the STP measurement experiment. Two STM probes (probe 1 and probe 2) are in contact with the sample surface applying a constant current. A third tip (probe 3) is positioned between the current probes and scans the sample surface to measure the local electrochemical potential ($\mu_{ec}$) at each point. The close proximity of the two current probes allows a sufficiently large voltage gradient detectable by the scanning probe even with a small applied current. (b) STM images showing a monolayer (ML)−bilayer (BL) graphene boundary. (c) STM images showing a ML−ML graphene boundary defined by substrate step. (d) STS taken near a ML−BL boundary at different locations as shown in the STM image in (e).**

found that the presence of GBs significantly increases the resistance in partially grown graphene islands.[14] The ambiguity in these findings arose from a lack of knowledge of the precise domain/grain morphology for the samples measured. While there are recent studies that produced maps of the electronic properties of graphene GBs using scanning tunneling microscope (STM)[21] and of graphene conductance using micro four-point probe and noncontact terahertz time-domain spectroscopy measurements,[22] a one-to-one correspondence between defect structures and transport properties is still lacking. Indeed, because of the large length-scale difference between the atomic-scale defect structures and transport functions whose variations range from atomic-scale to mesoscale, few techniques have the capability of probing the relationship between the two.

Here we combine conventional and novel microscopic techniques to bridge these length scales. With the use of a scanning tunneling potentiometry (STP) setup with a cryogenic four-probe STM as illustrated in Figure 1a, the spatial variation of the local electrochemical potential $\mu_{ec}(x,y)$ is resolved across individual grain (domain) boundaries on a graphene surface in the presence of a current. With STM and scanning electron microscope (SEM), we examine the boundary structure and electronic properties. Potential maps are then measured in regions spanning a specific type of boundary, yielding a spatial distribution of electrical conductivity. The relationship between structure and transport is extracted down to the atomic scale for each individual defect.

## RESULTS AND DISCUSSION

**Graphene Domain Boundaries on SiC.** First, we examine the structures of graphene domain boundaries, defined by changes in layer thickness and substrate steps in epitaxial graphene grown on a Si-faced SiC (0001) substrate.[2,23] Figure 1b is the STM image of a boundary between monolayer (ML) and bilayer (BL) graphene, clearly showing moiré pattern and atomic lattice of graphene with a background due to the $(6\sqrt{3} \times 6\sqrt{3})R30°$ reconstructed buffer layer.[24] The BL graphene appears much smoother than the ML. Because

the graphene layer is formed through the graphitization of SiC (0001), a ML−BL boundary almost always coincides with an underlying substrate step.[9] STM images on both sides of the step show that the lattice structure of graphene remains unchanged across the boundary, indicating a carpet-like growth mode covering the substrate step and terraces. The relation between the graphene lattice and the moiré pattern allows us to identify that the step runs primarily parallel to the [11$\bar{2}$0] direction of the SiC substrate just as the steps observed for the hydrogen etched SiC(0001) substrates.[25] The extra layer underneath the graphene carpet has a primarily armchair type of edge structure. On the same sample surface, ML−ML boundaries can also be identified, as defined purely by a substrate step. Figure 1c shows a ML−ML boundary with a ML graphene blankets across a monolayer substrate step.

The electronic properties of graphene boundaries are then examined by scanning tunneling spectroscopy (STS). Figure 1d shows the STS data measured across a ML−BL boundary as shown in Figure 1e. Far away from the boundary, STS spectrum taken on ML graphene shows a minimum at zero bias (spectrum 12 in Figure 1d), while the spectrum on BL graphene (spectrum 1 in Figure 1d) shows a distinct minimum around −0.373 eV as well as the minimum at zero bias, consistent with previous observations on similar materials.[25,26] The local minimum at zero bias is due to the suppression of electron tunneling to graphene states near Fermi level ($E_F$) and simultaneous giant enhancement of electronic tunneling at higher energies due to a phonon-mediated inelastic channel.[27] The minimum at −0.373 V fits well to the position of the Dirac point ($E_D$), which shifts with the doping concentration.[25] For ML graphene, a linear DOS with a minimum at $E_D = -(0.48 \pm 0.05)$ eV is expected.[25] However, the expected dip in the DOS in tunneling spectra corresponding to the Dirac point of ML graphene on SiC(0001) is overwhelmed by the underlying buffer layer.[25] Approaching the boundary from the BL side, the STS minima at $E_D$ clearly shift toward lower energies. As proposed previously by Low *et al.*, the carrier concentration can vary at the step edges due to increased distance and suppressed interactions between graphene and SiC.[9] As shown in Figure 1d, the local minimum corresponding to $E_D$ changes from 0.373 to 0.293 eV when moving the measuring site from 10 nm away to 1 nm away from the boundary. As a first order estimate of the doping, we can convert these Dirac point values to charge-carrier concentration using the equation $n = E_D^2/\pi\hbar^2 v_F^2$, where $\hbar$ is Planck's constant divided by $2\pi$, $n$ is the carrier concentration, and $v_F$ is the Fermi velocity ($v_F = 10^6$ m/s). The two values of $E_D$ yield n-type dopings of $1.0 \times 10^{13}$ cm$^{-2}$ in the bulk BL graphene and $6.3 \times 10^{12}$ cm$^{-2}$ at about 1 nm from the boundary. Less than 1 nm from the boundary, the $E_D$ minimum merges with the zero bias minimum and thus is not resolved by STS, indicating a much lower carrier concentration in close proximity (<1 nm) of the boundary.

Figure 2 shows the potential distribution maps of the area near a ML−BL boundary (a and b) and a ML−ML boundary (c and d) with a source current flowing either from right to left side (a and c) of the boundary or in the reverse direction (b and d). In the potential map, the measured quantity $\mu_{ec}(x,y)$ characterizes the electronic energy level filling in a nonequilibrium situation and its gradient describes the local electric field driving the electric transport.[28] When current flows from the right side of the boundary to the left, a clear potential drop occurs at the step edge, with a lower potential on left terrace and higher potential on the right terrace. When the current flows from the left side of the boundary to the right, the relative potentials between the two domains are reversed. A clear potential drop is observed both at the ML-BL and ML-ML boundaries.

On the basis of the 2D potential distribution, the direction and magnitude of the component of the local transport field $\mathbf{E}(x,y)$ can be extracted using the relation, $\mathbf{E} = -(1/e)\nabla\mu_{ec}(x,y)$. The field is computed numerically along the $x$, $y$ directions from the STP data array. For a potential map acquired near a ML−BL boundary as shown in Figure 3a, the field is visually displayed in Figure 3b using a quiver plot, with the length of the arrow indicating the magnitude and the head pointing along the direction of the field. This 2D distribution analysis brings out two points. The apparent width of boundary displayed in the potential maps has a much larger spatial extent compared to the topology transition which is atomically sharp. This is consistent with the observation of the gradual reduction of chemical potential near the boundary (Figure 1d). Second, the electric field is very strong near the boundary but weak on the terraces, and shows a clear variation along the boundary, causing a nonuniform current density distribution across the boundary.

The conductivity can be extracted from the potential map by solving the conduction equations. The current conservation condition is

$$\nabla \cdot \mathbf{j} = \frac{\partial}{\partial x}(\sigma_x E_x) + \frac{\partial}{\partial y}(\sigma_y E_y) = 0 \qquad (1)$$

Additional equations are obtained by assuming $\nabla \times \mathbf{j} = 0$ which means that there are no closed current loops. We write out this condition as

$$\oint (\sigma_x E_x \, dx + \sigma_y E_y \, dy) = 0 \qquad (2)$$

By solving these equations numerically using appropriate boundary conditions, we obtain the conductivity for each position where the electrochemical potential is measured. Figure 3c shows the map of

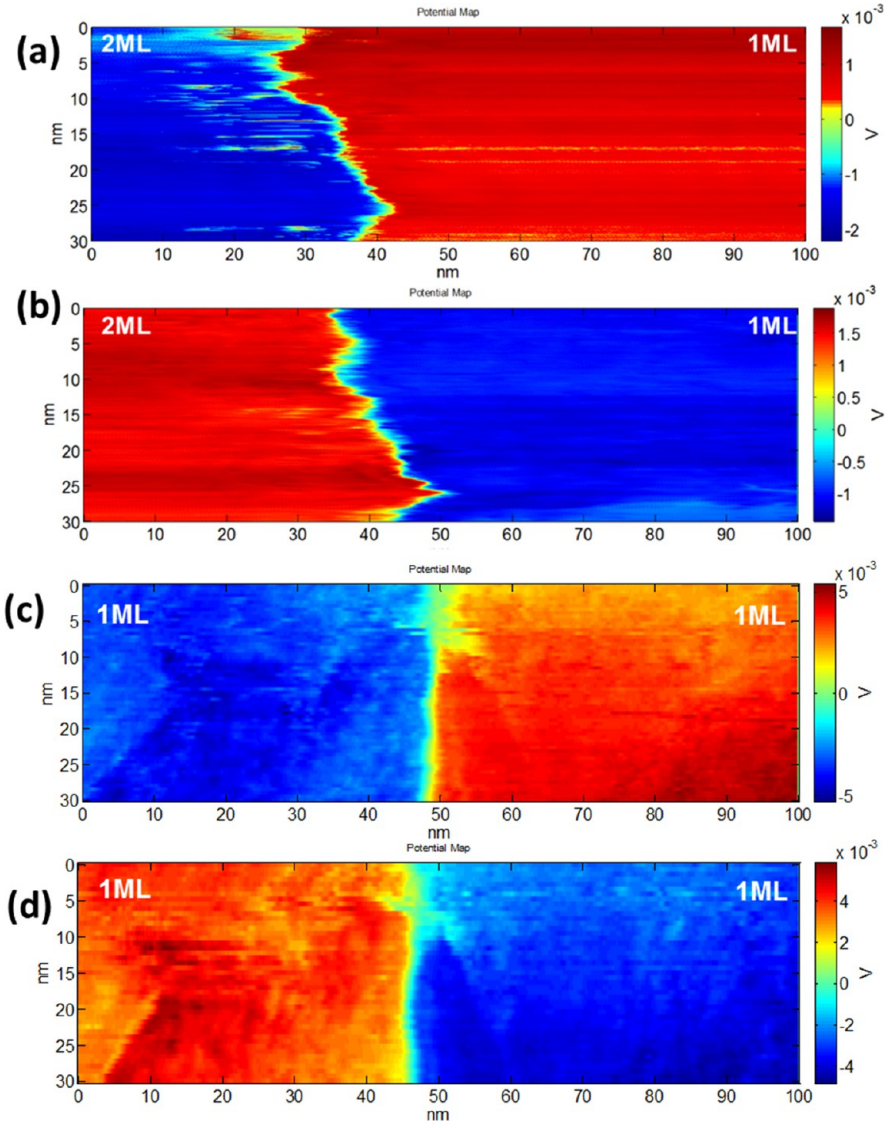


**Figure 2. Spatially resolved electrochemical potential maps measured at domain boundaries of epitaxial graphene on a SiC substrate: (a) ML−ML with forward (147 $\mu$A current from ML to BL); (b, ML−BL with reversed bias condition (147 $\mu$A current from BL to ML); (c) ML−ML with forward (154 $\mu$A current from ML to B); (d, ML−ML with reversed bias condition (154 $\mu$A current from BL to ML).**

the conductivity component along the source current direction. The conductivity on the terraces is very uniform, with a clearly depressed conductivity at the boundary. Because we do not know all the boundary conditions to determine the total current within the region of measurement, it is not possible to uniquely determine the conductivities from the potential distribution alone. Therefore, the calculated conductivity values in Figure 3c are relative to an unknown scale. Ji *et al.* estimated the local current density based on the measured total current density using a Laplace equation.[8] Here we instead measure the conductivity of each terrace across the boundary independently using the four-probe STM,[29] which offers a model-independent reference "standard" to normalize the conductivity map. The graphene sample can be regarded as infinitely large in comparison with the probe spacing for four-point contact measurements (<2 $\mu$m). For a uniform 2D conductor, the measured resistance is related to the surface conductivity ($\sigma_s$) by

$$R_{2D} = \frac{1}{2\pi\sigma_s}\left|\ln\frac{s_{13}s_{24}}{s_{23}s_{14}}\right| \quad (3)$$

where $s_{ij}$ is the separation between probes $i$ and $j$. By locating all four probes onto the ML graphene terrace, we find the conductivity to be (1.2 $\pm$ 0.2) mS as shown in Figure S1 in the Supporting Information. By comparing this independently measured conductivity and the averaged ML conductivity derived from the potential map, we can quantify the scale bars in the conductivity maps in Figure 3c. Note that eq 3 is only rigorously valid for a uniform 2D system. Under the conditions that the conductivity variation between different domains is not very large and that the probe spacing is

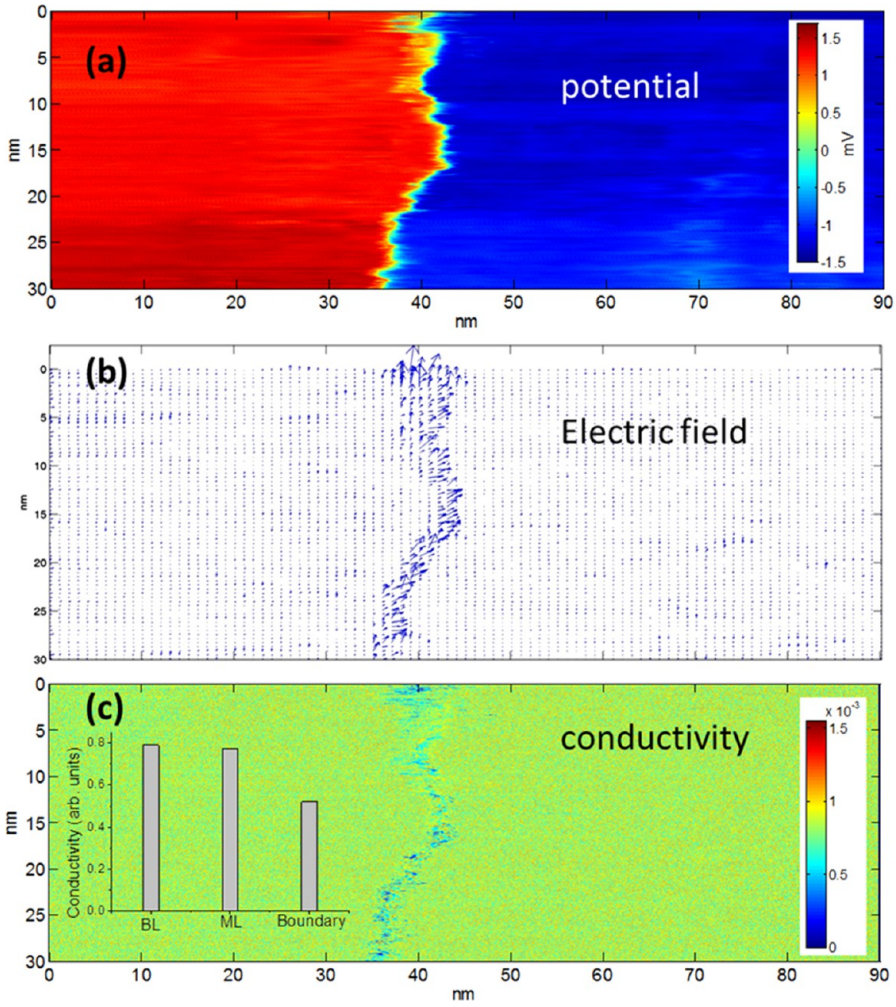


**Figure 3. Spatially resolved electron transport behaviors revealed by STP measurements at domain boundaries of epitaxial graphene on a SiC substrate. (a) Electrochemical potential map measured at a ML−BL graphene boundary. (b) Electric field distribution derived from the potential map in (a). (c) Conductivity map derived from the potential map in a. Inset, histogram showing the relative conductivity of ML, BL, and their boundary.**

smaller than the 2D domain size, this equation provides a good approximation to estimate the conductivity of the domain. The error should be proportional to the fluctuation in the conductivity between domains which contributes to an overall error bar in our 2D conductivity map, but should have minimal impact on the estimate of the grain boundary conductance.

Table 1 summarizes the measured conductivities of ML and BL graphene, and different boundaries on SiC substrate. The following points are noted: (i) The resistance of ML−BL heterojunction is higher than ML−ML homojunctions, while BL graphene has a similar bulk resistance as ML. On the basis of the measured graphene conductivity and the carrier concentration, the carrier mobility can be estimated as $\mu = \sigma/ne \approx$ 813 $cm^2/V \cdot s$. Previous studies by Ji *et al.*[8] attributed the higher resistance at ML−BL boundary to the intrinsic wave function mismatch at the junction of ML and BL graphene. (ii) The resistance of the boundary over a higher step is significantly greater than a similar boundary over a lower step. The resistance change is closely related to the change in the width of the transition region for boundaries associated with different step heights.

The values of the transition region width in Table 1 are measured directly from potential maps across the boundary. These measurements reveal an electronic transition region arising from the doping concentration change near the boundary as shown in STS (Figure 1d) and the boundary scattering effect as indicated by the electric field distribution (Figure 3b). The electronic transition region coincides with a structural transition region near the step edge, although the latter is usually much narrower in width, *e.g.*, an atomically sharp transition shown by STM images in Figure.1. In fact, the structural transition region was experimentally examined with cross-sectional TEM images[30,31] where a deformation region of graphene is seen and graphene pulls away from the substrate near the substrate step of SiC. Theoretical considerations suggest that in the deformation region, the substrate-induced doping in graphene is substantially

**TABLE 1. Electrical Conductivity of Graphene and Domain Boundaries Across Substrate Steps on SiC Measured at 81 K**

| | | conductivity (mS) | | | | |
|---|---|---|---|---|---|---|
| domain boundary type | current flow direction | ML | BL | boundary | transition width (nm) | boundary resistance ($\Omega \cdot \mu$m) |
| BL/ML with step 1.0 nm high | BL to ML | 1.2 | 1.3 | 0.10 | 9 | 90 |
| | ML to BL | 1.2 | 1.3 | 0.13 | 10 | 77 |
| BL/ML with step 0.8 Å high | BL to ML | 1.2 | 1.2 | 0.65 | 1.2 | 1.9 |
| | ML to BL | 1.2 | 1.3 | 0.84 | 1.2 | 1.4 |
| ML/ML with step 2.5 Å high | ML to ML | 1.2 | | 1.1 | 1.3 | 1.2 |

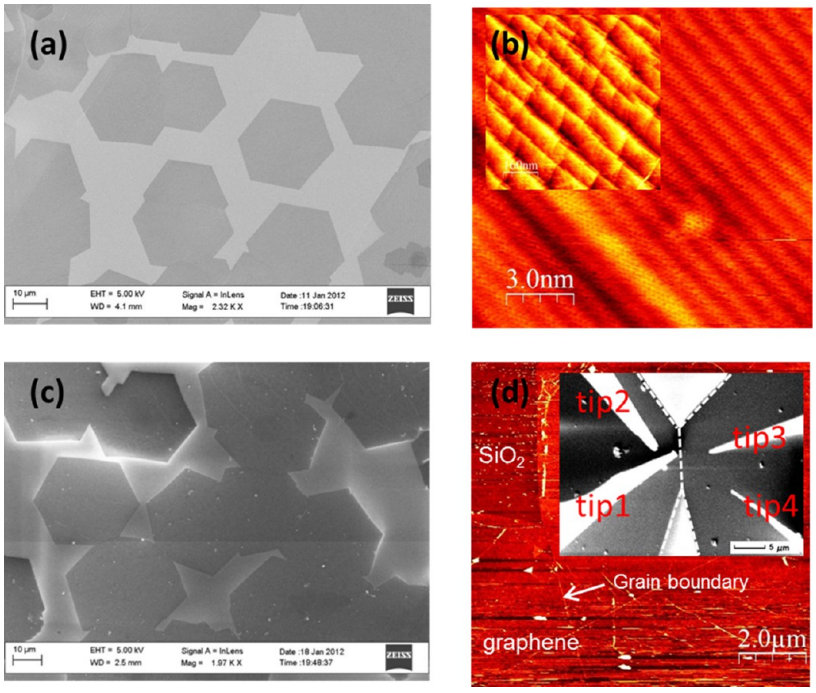


**Figure 4. Characterization of CVD graphene grown on a Cu foil substrate. (a) SEM image showing coalesced grains on Cu foil. (b) STM images showing graphene textures and atomic structures on Cu foil. Inset, large range STM image. (c) SEM image of graphene after transferring to $SiO_2$. (d) AFM image showing the grain boundary of two adjacent grains. Inset, SEM image with four STM tips located near a grain boundary. Dash lines indicate the edges of graphene grains.**

reduced due to the suppressed interaction between graphene and the substrate.[9] Our STS data in Figure 1d provide a direct visual evidence of such a carrier depletion region at the boundary.

**Grain Boundaries in CVD Graphene.** We now turn to the GBs in CVD graphene. The growth of hexagonal graphene domains on Cu foil by atmospheric pressure CVD was described previously by Vlassiouk *et al.*[11] The graphene islands are shown in SEM image in Figure 4a as large hexagonal patches of single ML graphene, over 10 $\mu$m across, on the copper foil surface. Minor density of bi- and trilayers (darker areas in Figure 4a) is easily resolved by SEM and further measurements were performed on single layer graphene crystals. Since graphene growth on Cu foil in our approach leads to the formation of randomly orientated grains, the coalescence of neighboring graphene grains forms boundaries where grains with different orientation angles meet. From SEM images, the angle between the individual hexagonal graphene patches can be conveniently measured. The atomic structures of graphene on Cu foil is resolved in STM image shown in Figure 4b, and large-scale textures can be seen (inset of Figure 4b) that reflects the features on Cu foil in the conformal graphene film. The edges of graphene grains are mostly seen parallel to a zigzag direction in the graphene lattice, as previously observed on similar materials.[14] The graphene film is then transferred to a $SiO_2$/Si substrate and annealed at 600 °C in UHV to clean the surface. Raman spectra taken at different locations confirm that the substrate is mostly covered by ML graphene. Some debris are not removed in sample preparation process and remain on the surface as shown in SEM image in Figure 4c and AFM image in Figure 4d. On the basis of SEM and AFM images, several misorientation angles of 9°, 12°, 14°, and 21° between graphene grains have been identified. Note that on the atomic and microscopic scales the grain boundary is

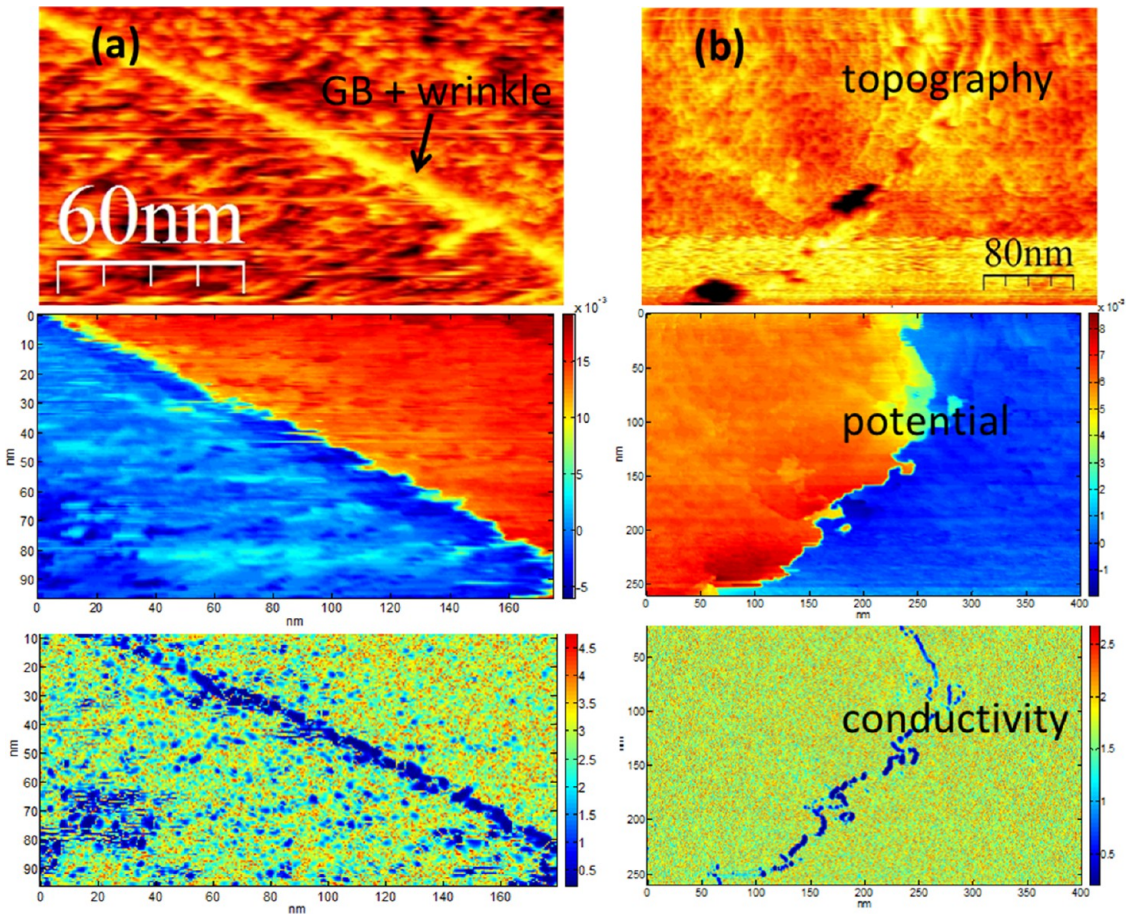


**Figure 5. Spatially resolved electron transport behaviors revealed by STP measurements CVD graphene on $SiO_2$. (a) Electrochemical potentials, electric field distributions, and conductivity map, respectively, measured at a graphene grain boundary (14°) coinciding with structural wrinkles. (b) Electrochemical potentials, electric field distributions, and conductivity map, respectively, measured at two graphene grain boundaries (9° and 21°) without structural wrinkles.**

not always a straight line and usually deviates from the macroscopic angle (global angle) as the crystal structure minimizes energy during the growth process. The deviations are very small in comparison to the global angle measured from the SEM image. The surface also displays wrinkles induced by thermal stress and substrate steps[32] which often coincide with the grain boundaries.

Electrical transport is first measured by four-point contact method with the 4-probe STM near a single grain boundary, as shown in the inset of Figure 4d. The movable four STM probes can contact each grain to allow simultaneous measurements of both intra-grain (within the grain) and inter-grain (across the GB) transport.[29] The resistance obtained were, for the left grain $R_L$ = 408 Ω, right grain $R_R$ = 549 Ω, and across grain boundary $R_{GB}$ = 760 Ω, while keeping the probe distances approximately the same. Using eq 3, we can derive a conductivity for left and right grains as 0.28 and 0.24 mS, respectively. This measurement is similar to that measured on multiterminal devices fabricated from two coalescent graphene grains,[14] confirming that the grain boundary provides an 'extra' resistance. The measured conductivities for 14 individual grains fall in a range of (0.20−0.41) mS, corresponding to roughly $(5-11)e^2/h$. Note, the minimum DC conductivity of graphene on $SiO_2$ of $\sigma_{min} = (2-12)e^2/h$ found by Tan *et al.*[33] and an earlier study[34] reporting $\sigma_{min} = 4e^2/h$.

The spatially resolved STP maps for grain boundaries with (a) and without (b) wrinkles are shown in Figure 5, where the top panel shows topography images, middle panel shows corresponding $\mu_{ec}(x,y)$, and bottom panel shows the extracted conductivity component along the current direction. Clearly potential drops and reduced conductivity are observed at both grain boundary locations in comparison with the uniform grain regions. To further verify the effect of wrinkles on conductivity, we have measured the conductivity of a wrinkle that is 20 nm in width and 2 nm in height in the absent of a GB, and obtained a conductivity value (0.1 mS) approximately 40% of that of the bulk grain. The corresponding resistance (200 Ω·μm) agrees very well with a calculated value (200−300 Ω·μm) for graphene wrinkles from Zhu *et al.*[35] The wrinkle at GB site is much narrower and only plays a secondary role in the increase of the GB resistance in comparison with GB itself.

Table 2 summarizes the conductivity values measured at different types of grain boundary. All GBs show

**TABLE 2. Electrical conductivity of graphene and grain boundaries on $SiO_2$ measured at 81 K**

| Boundary type | Misorientation Angle (°) | Ratio of conductivity (Boundary/Grain) | GB transition width (nm) | GB resistance (ohm·μm) |
|---|---|---|---|---|
| GB | 9 | 0.32 | 3.4 | 42.5 |
| GB with wrinkle | 12 | 0.24 | 3.3 | 55 |
| GB with wrinkle | 12 | 0.18 | 5 | 111 |
| GB with wrinkle | 12 | 0.14 | 4.4 | 125.7 |
| GB | 14 | 0.33 | 5.8 | 77.3 |
| GB with wrinkle | 14 | 0.26 | 6.2 | 95.4 |
| GB with wrinkle | 14 | 0.19 | 4.7 | 98.9 |
| GB | 21 | 0.12 | 4.3 | 143.3 |
| Wrinkle | | 0.40 | 20 | |

effective conductivity less than one-third of the bulk conductivity of a grain. For GBs without wrinkles (highlighted with blue font in Table 2), at first glance there seems to be a positive correlation between misorientation angle and the GB resistance, and that wrinkles at GB seem to further increase the GB resistance.[36] However, our analysis below shows that the deciding factor for GB resistance is actually the width of the electronic transition region at the GB. Similar to the graphene on SiC, the electronic transition region at GB measured from STP map is much wider than the atomically sharp structural transition shown by TEM images.[20] The GB resistance measured here is more than an order of magnitude smaller than those obtained by Tsen *et al.*[37] with lithographically fabricated contacts where processing-induced contaminations could potentially increase GB resistance values.

Yazyev and Louie[38] have calculated the conductance of a GB and found the conductance would be nearly 70−80% of the bulk graphene conductance. In contrast, our measured grain boundary conductance is less than one-third of the bulk conductance, far below the theoretical prediction. Thus, the measured GB conductance values cannot be explained by scattering from a coherent and atomically sharp boundary. As evident from the spatial dependent conductance maps, there is a relatively wide electronic transition region at grain boundaries. The transition region can have different charge density due to *e.g.*, self-doping,[39] and very different amount of disorder, in particular vacancies,[40] which can contribute to a larger resistance than the lattice mismatch alone. Such a transition region has been analyzed by Castro Neto *et al.*,[39] who found that the combination of localized defects and the lack of electron−hole symmetry around the Dirac points lead to self-doping, *i.e.*, shifting of the Fermi energy in comparison with the clean graphene regions. Van Tuan *et al.*[41] recently showed that the grain boundary exhibits large charge fluctuations over the width of approximately 1 nm with the maximum local carrier density 1 order of magnitude greater than the average density. This would suggest that the Fermi wave vector in the transition region is much larger than in the graphene domains.

To analyze the scattering effect of the transition region, we assume that the self-doping arises from an attractive potential, which we model as square well. The depth of the well will lead to a different Fermi wave vector for electron wave functions inside the transition region than in bulk grains. This leads to a variation in the resistance of the transition region in accordance with its transmission probability,

$$T = \frac{1}{1 + \dfrac{(k_F^2 - k_{F,T}^2)^2 \sin^2 k_{F,T} d}{4 k_F^2 k_{F,T}^2}} \quad (4)$$

where $d$ is the width of the transition region, $k_{F,T}$ is the Fermi wave vector of the electron wave function in the transition region, and $k_F$ is the Fermi wave vector in the bulk grain region. The precise form of this transmission is not so important for our argument, since other shapes for the potential profiles in the transmission region will similarly lead to a transmission function with oscillatory behavior as a function of $d$. For a line boundary the transmission needs to be integrated over all incident angles, which should truncate at a maximum transverse wave vector value of $k_F$, to yield transmission per unit length. We approximate this quantity by simply multiplying the transmission probability with $k_F$. The line resistance is then found from the Landauer formula,

$$R_{trans} = \frac{h}{2e^2 T k_F} = \frac{h}{2e^2}\left[\frac{1}{k_F} + \frac{(k_F^2 - k_{F,T}^2)^2}{4 k_F^3 k_{F,T}^2} \sin^2 k_{F,T} d\right] \quad (5)$$

The second effect, that of disorder, is not easily captured in a quantum transport model. When there is

a finite electron scattering lifetime $\tau$, a naïve application of the mean-field approximation makes the wave vector in the transition region complex,

$$k_1 = k_{F,T} + \frac{i}{v_F \tau} \quad (6)$$

where $v_F$ is the Fermi velocity. Using this complex wave vector in eq 5 would lead to an exponentially growing resistance. However, such a complex wave vector does not take into account the so-called vertex corrections, which are due to current carried by electrons scattered into a given conduction channel (*i.e.*, the scatter-in terms). The rigorous computation of the vertex corrections is cumbersome. Here we employ a simple approximate procedure[42] whereby the transmission coefficient is computed with a real wave vector, which by itself underestimates the boundary resistance, and the diffusive contribution is added back as a separate Ohmic term over the thickness of the transition region. This procedure is exact for the model of free electrons with random point scatterers.[43]

The diffusive contribution is thus calculated as

$$R_{dif} = \frac{d}{\sigma_{dif}} = \frac{hd}{2e^2 v_F k_{F,T} \tau} \quad (7)$$

Combining the two contributions, the total resistance is

$$R_{GB} = \frac{h}{2e^2}\left[\frac{1}{k_F} + \frac{(k_F^2 - k_{F,T}^2)^2}{4k_F^3 k_{F,T}^2}\sin^2 k_{F,T}^2 d + \frac{d}{k_{F,T} v_F \tau}\right] \quad (8)$$

The gate voltage dependence of this result is consistent with report from Tsen *et al.*[37] if we assume that $k_{F,T} \propto k_F$ when both change with the gate voltage, thus $R_{GB}$ scales with $1/k_F$ similar to the bulk domain resistance. Note that Tsen *et al.* only have data for a single transition region width, whereas eq 8 has explicit dependence on both the wave vectors and the width of the transition region. To reduce the number of parameters in eq 8, we simplify the diffusive term to the limiting case of a resistance corresponding to the minimum conductivity for graphene,[34]

$$R_{dif} = \frac{d}{\sigma_{min}} = \frac{hd}{4e^2} \quad (9)$$

The total GB resistance is then

$$R_{GB} = \frac{h}{2e^2}\left[\frac{1}{k_F} + \frac{(k_F^2 - k_{F,T}^2)^2}{4k_F^3 k_{F,T}^2}\sin^2 k_{F,T}^2 d + \frac{1}{2}d\right] \quad (10)$$

In Figure S2 of the Supporting Information we plot all measured GB resistance data for CVD graphene as a function of transition region width. There is no apparent difference between data with and without wrinkles. In this figure we also show two different fits, one using eq 10 which includes the diffusive resistance due to disorder (blue curve), and the second without the diffusive term (red curve). Even without including the diffusive term, the model captures the overall trend of the resistance change as a function of the transition region width. This means that the change of the electron wave vector in the transition region is the largest source of GB resistance. By fitting the resistance data to eq 10, we find parameters $k_F = 0.366\ nm^{-1}$ (in the bulk grain region) and $k_{F,T} = 1.07\ nm^{-1}$ (in the transition region). This gives an estimated Fermi energy measured from the Dirac point as 241 meV in the bulk region, and an estimated bulk carrier density of $4.3 \times 10^{12} cm^{-2}$. Using this number and measured bulk conductivity in the range (0.20−0.41) mS, we estimate the carrier mobility to be s $(2.9-6.0) \times 10^3\ cm^2/V\cdot s$. The carrier density in the boundary region can also be estimated by using the value $k_{F,T} = 1.07\ nm^{-1}$, which gives the carrier density of $3.6 \times 10^{13}\ cm^{-2}$. This is a very high carrier density compared to the value in the bulk, consistent with the presence of self-doping[39] and previous observation at GB.[41]

## CONCLUSION

In summary, we have mapped out the spatial distributions of electrical conductivity near the structural defects in epitaxial graphene grown on SiC and CVD graphene on Cu subsequently transferred to a $SiO_2$ substrate. With the combination of STM and multiple-probe potentiometry techniques, the transport properties have been correlated to the structures and electronic properties for individual domain or grain boundaries in graphene. For epitaxial graphene, the resistance of ML−BL heterojunction is higher than that of ML−ML homojunctions while BL graphene has a similar resistance as ML, the resistance of the boundary with a higher step is significantly greater than a similar boundary on a lower step, and the increased resistance is associated with the reduced charge transfer from the substrate near the step edge. For CVD graphene, the measured GB resistance changes with GB transition width and can be quantitatively modeled by considering charge density variation and disorder scattering in the transition region.

## METHODS

**STM and STP Measurements.** Our experiments were carried out at 81 K with a Unisoku cryogenic four-probe STM controlled by electronics from RHK and Nanonis with a base pressure of $3 \times 10^{-10}$ Torr and electrochemically etched tungsten tips.[29,44] Two approaches have been used to separate signals from topography and potentiometry. The first, used in the originalexperiments by Muralt *et al.*,[45] employs ac current to control the tip−surface separation and dc current to identify the voltage drop across the sample which can be distinguished using a lock-in technique. With this approach, the topography and potentiometry signals are measured simultaneously. The second approach, introduced by Feenstra and co-workers,[46,47] uses an interrupted feedback, first measuring the surface topography, and then

retracing that topography with the feedback off to determine the potentiometry. Topology is determined with the feedback loop to the z piezo active. The feedback loop is then interrupted and the tip (or sample) bias used for topographic scanning is switched off. With the tip held at a fixed position, $I-V$ characteristics are quickly measured before drift becomes significant (on the order of a few seconds). The recorded $I-V$ curve is postprocessed by fitting with a linear equation and the bias voltage at zero tunneling current is extracted from the fit. This zero current bias voltage is the potential value at that point on the sample. This process is repeated at each point on the grid to build up the potential map of the surface.

**Graphene Growth on SiC.** The graphite heater consisted of a bow-tie shaped graphite plate with 1 mm thickness and narrow neck measuring about 14 mm wide and 20 mm long. A 1 cm × 1 cm sample rests on this narrow strip, and is heated by currents of typically 200 A passed through the strip. Water-cooled copper clamps and electrical feedthroughs supply the current, and the heater is contained in an ultrahigh-vacuum chamber. The SiC graphene growth procedure starts with hydrogen etching at 1620 °C for 3 min followed by the graphene growth at 1590 °C for 30 min in 1 atm argon environment. The SiC Graphene samples were grown on the Si face of 4H-SiC. The Si face of SiC allows for more controlled growth of the graphene thickness due to the Si face initially growing a buffer layer that acts as a template for the graphene formation as the Si is sublimed from the surface.

**CVD Growth of Graphene on Cu Foil and Film Transfer to $SiO_2$/Si.** Our growth recipe is similar to those previously published.[11,15] In short, we grew graphene by atmospheric CVD process. Before the growth, 125 $\mu$m thick copper foil from Nimrod Hall Copper Foil Company, was electropolished in concentrated $H_3PO_4$. The foils were loaded in quartz tube and annealed for 1 h at 1000 °C under 500 sccm flow of 2.5% $H_2$ in Ar atmosphere. The growth was performed by addition of 8 sccm 0.1% $CH_4$ in Ar mixture keeping hydrogen partial pressure unchanged. After 90 min of growth, the furnace was quickly cooled to the room temperature. Graphene transfer was performed by spin coating Microchem 950 A4 PMMA solution (1500 rpm, 45 s). Copper foil was etched by 1 M $FeCl_3$ solution, and the floating PMMA was washed with DI water and transferred to Si/$SiO_2$ wafer. PMMA was dissolved in acetone.

*Conflict of Interest:* The authors declare no competing financial interest.

*Acknowledgment.* This research was conducted at the Center for Nanophase Materials Sciences, which is sponsored at Oak Ridge National Laboratory by the Office of Basic Energy Sciences, U.S. Department of Energy. The support (G.H. and R.M.F.) from the National Science Foundation is also acknowledged. We thank G. Gu for discussions and S. Jesse for assistance with data processing of this work.

*Supporting Information Available:* Additional experimental data and analysis graphs. This material is available free of charge *via* the Internet at http://pubs.acs.org.

## REFERENCES AND NOTES

1. Novoselov, K. S.; Falko, V. I.; Colombo, L.; Gellert, P. R.; Schwab, M. G.; Kim, K. A Roadmap for Graphene. *Nature* **2012**, *490*, 192–200.
2. Berger, C.; Song, Z.; Li, T.; Li, X.; Ogbazghi, A. Y.; Feng, R.; Dai, Z.; Marchenkov, A. N.; Conrad, E. H.; First, P. N.; *et al.* Ultrathin Epitaxial Graphite: 2D Electron Gas Properties and a Route toward Graphene-based Nanoelectronics. *J. Phys. Chem. B* **2004**, *108*, 19912–19916.
3. Li, X.; Cai, W.; An, J.; Kim, S.; Nah, J.; Yang, D.; Piner, R.; Velamakanni, A.; Jung, I.; Tutuc, E.; *et al.* Large-Area Synthesis of High-Quality and Uniform Graphene Films on Copper Foils. *Science* **2009**, *324*, 1312–1314.
4. McEuen, P. L.; Bockrath, M.; Cobden, D. H.; Yoon, Y.-G.; Louie, S. G. Disorder, Pseudospins, and Backscattering in Carbon Nanotubes. *Phys. Rev. Lett.* **1999**, *83*, 5098–5101.
5. Dimitrakopoulos, C.; Grill, A.; McArdle, T. J.; Liu, Z.; Wisnieff, R.; Antoniadis, D. A. Effect of SiC Wafer Miscut Angle on the Morphology And Hall Mobility of Epitaxially Grown Graphene. *Appl. Phys. Lett.* **2011**, *98*, 222105.
6. Bryan, S. E.; Yang, Y.; Murali, R. Conductance of Epitaxial Graphene Nanoribbons: Influence of Size Effects and Substrate Morphology. *J. Phys. Chem. C* **2011**, *115*, 10230–10235.
7. Park, J.; He, G.; Feenstra, R. M.; Li, A.-P. Atomic-Scale Mapping of Thermoelectric Power on Graphene: Role of Defects and Boundaries. *Nano Lett.* **2013**, *13*, 3269–3273.
8. Ji, S.-H.; Hannon, J. B.; Tromp, R. M.; Perebeinos, V.; Tersoff, J.; Ross, F. M. Atomic-Scale Transport in Epitaxial Graphene. *Nat. Mater.* **2012**, *11*, 114–119.
9. Low, T.; Perebeinos, V.; Tersoff, J.; Avouris, P. Deformation and Scattering in Graphene over Substrate Steps. *Phys. Rev. Lett.* **2012**, *108*, 096601.
10. Li, X.; Magnuson, C. W.; Venugopal, A.; Tromp, R. M.; Hannon, J. B.; Vogel, E. M.; Colombo, L.; Ruoff, R. S. Large-Area Graphene Single Crystals Grown by Low-Pressure Chemical Vapor Deposition of Methane on Copper. *J. Am. Chem. Soc.* **2011**, *133*, 2816–2819.
11. Vlassiouk, I.; Regmi, M.; Fulvio, P.; Dai, S.; Datskos, P.; Eres, G.; Smirnov, S. Role of Hydrogen in Chemical Vapor Deposition Growth of Large Single-Crystal Graphene. *ACS Nano* **2011**, *5*, 6069–6076.
12. Wofford, J. M.; Nie, S.; McCarty, K. F.; Bartelt, N. C.; Dubon, O. D. Graphene Islands on Cu Foils: The Interplay between Shape, Orientation, and Defects. *Nano Lett.* **2010**, *10*, 4890–4896.
13. Wood, J. D.; Schmucker, S. W.; Lyons, A. S.; Pop, E.; Lyding, J. W. Effects of Polycrystalline Cu Substrate on Graphene Growth by Chemical Vapor Deposition. *Nano Lett.* **2011**, *11*, 4547–4554.
14. Yu, Q.; Jauregui, L. A.; Wu, W.; Colby, R.; Tian, J.; Su, Z.; Cao, H.; Liu, Z.; Pandey, D.; Wei, D.; *et al.* Control and Characterization of Individual Grains and Grain Boundaries in Graphene Grown by Chemical Vapour Deposition. *Nat. Mater.* **2011**, *10*, 443–449.
15. Vlassiouk, I.; Fulvio, P.; Meyer, H.; Lavrik, N.; Dai, S.; Datskos, P.; Smirnov, S. Large Scale Atmospheric Pressure Chemical Vapor Deposition of Graphene. *Carbon* **2013**, *54*, 58–67.
16. Robinson, Z. R.; Tyagi, P.; Mowll, T. R.; Ventrice, C. A., Jr.; Hannon, J. B. Argon-Assisted Growth of Epitaxial Graphene on Cu(111). *Phys. Rev. B* **2012**, *86*, 235413.
17. Gao, L.; Guest, J. R.; Guisinger, N. P. Epitaxial Graphene on Cu(111). *Nano Lett.* **2010**, *10*, 3512–3516.
18. Liu, Y.; Yakobson, B. I. Cones, Pringles, and Grain Boundary Landscapes in Graphene Topology. *Nano Lett.* **2010**, *10*, 2178–2183.
19. Yazyev, O. V.; Louie, S. G. Topological Defects in Graphene: Dislocations and Grain Boundaries. *Phys. Rev. B* **2010**, *81*, 195420.
20. Huang, P. Y.; Ruiz-Vargas, C. S.; van der Zande, A. M.; Whitney, W. S.; Levendorf, M. P.; Kevek, J. W.; Garg, S.; Alden, J. S.; Hustedt, C. J.; Zhu, Y.; *et al.* Grains and Grain Boundaries in Single-Layer Graphene Atomic Patchwork Quilts. *Nature* **2010**, *469*, 389–392.
21. Koepke, J. C.; Wood, J. D.; Estrada, D.; Ong, Z.-Y.; He, K. T.; Pop, E.; Lyding, J. W. Atomic-Scale Evidence for Potential Barriers and Strong Carrier Scattering at Graphene Grain Boundaries: A Scanning Tunneling Microscopy Study. *ACS Nano* **2012**, *7*, 75–86.
22. Buron, J. D.; Petersen, D. H.; Bøggild, P.; Cooke, D. G.; Hilke, M.; Sun, J.; Whiteway, E.; Nielsen, P. F.; Hansen, O.; Yurgens, A.; *et al.* Graphene Conductance Uniformity Mapping. *Nano Lett.* **2012**, *12*, 5074–5081.
23. Luxmi; Srivastava, N.; He, G.; Feenstra, R. M.; Fisher, P. J. Comparison of Graphene Formation on C-face and Si-face SiC {0001} Surfaces. *Phys. Rev. B* **2010**, *82*, 235406.
24. Riedl, C.; Starke, U.; Bernhardt, J.; Franke, M.; Heinz, K. Structural Properties of the Graphene-SiC(0001) Interface as a Key for the Preparation of Homogeneous Large-Terrace Graphene Surfaces. *Phys. Rev. B* **2007**, *76*, 245406.
25. Lauffer, P.; Emtsev, K. V.; Graupner, R.; Seyller, T.; Ley, L. Atomic and Electronic Structure of Few-Layer Graphene on SiC(0001) Studied with Scanning Tunneling Microscopy and Spectroscopy. *Phys. Rev. B* **2008**, *77*, 155426.

26. Zhang, Y.; Brar, V. W.; Wang, F.; Girit, C.; Yayon, Y.; Panlasigui, M.; Zettl, A.; Crommie, M. F. Giant Phonon-Induced Conductance in Scanning Tunnelling Spectroscopy of Gate-Tunable Graphene. *Nat. Phys.* **2008**, *4*, 627–630.
27. Wehling, T. O.; Grigorenko, I.; Lichtenstein, A. I.; Balatsky, A. V. Phonon-Mediated Tunneling into Graphene. *Phys. Rev. Lett.* **2008**, *101*, 216803.
28. Chu, C. S.; Sorbello, R. S. Phase-Sensitive Scanning Tunneling Potentiometry and the Local Transport Field in Mesoscopic Systems. *Phys. Rev. B* **1990**, *42*, 4928–4939.
29. Kim, T. H.; Zhang, X. G.; Nicholson, D. M.; Evans, B. M.; Kulkarni, N. S.; Radhakrishnan, B.; Kenik, E. A.; Li, A. P. Large Discrete Resistance Jump at Grain Boundary in Copper Nanowire. *Nano Lett.* **2010**, *10*, 3096–3100.
30. Nagase, M.; Hibino, H.; Kageshima, H.; Yamaguchi, H. Local Conductance Measurements of Double-Layer Graphene on SiC Substrate. *Nanotechnology* **2009**, *20*, 445704.
31. Nicotra, G.; Ramasse, Q. M.; Deretzis, I.; La Magna, A.; Spinella, C.; Giannazzo, F. Delaminated Graphene at Silicon Carbide Facets: Atomic Scale Imaging and Spectroscopy. *ACS Nano* **2013**, *7*, 3045–3052.
32. Pan, Z.; Liu, N.; Fu, L.; Liu, Z. Wrinkle Engineering: A New Approach to Massive Graphene Nanoribbon Arrays. *J. Am. Chem. Soc.* **2011**, *133*, 17578–17581.
33. Tan, Y. W.; Zhang, Y.; Bolotin, K.; Zhao, Y.; Adam, S.; Hwang, E. H.; Das Sarma, S.; Stormer, H. L.; Kim, P. Measurement of Scattering Rate and Minimum Conductivity in Graphene. *Phys. Rev. Lett.* **2007**, *99*, 246803.
34. Novoselov, K. S.; Geim, A. K.; Morozov, S. V.; Jiang, D.; Katsnelson, M. I.; Grigorieva, I. V.; Dubonos, S. V.; Firsov, A. A. Two-Dimensional Gas of Massless Dirac Fermions in Graphene. *Nature* **2005**, *438*, 197–200.
35. Zhu, W.; Low, T.; Perebeinos, V.; Bol, A. A.; Zhu, Y.; Yan, H.; Tersoff, J.; Avouris, P. Structure and Electronic Transport in Graphene Wrinkles. *Nano Lett.* **2012**, *12*, 3431–3436.
36. Xu, K.; Cao, P.; Heath, J. R. Scanning Tunneling Microscopy Characterization of the Electrical Properties of Wrinkles in Exfoliated Graphene Monolayers. *Nano Lett.* **2009**, *9*, 4446–4451.
37. Tsen, A. W.; Brown, L.; Levendorf, M. P.; Ghahari, F.; Huang, P. Y.; Havener, R. W.; Ruiz-Vargas, C. S.; Muller, D. A.; Kim, P.; Park, J. Tailoring Electrical Transport Across Grain Boundaries in Polycrystalline Graphene. *Science* **2012**, *336*, 1143–1146.
38. Yazyev, O. V.; Louie, S. G. Electronic Transport in Polycrystalline Graphene. *Nat. Mater.* **2010**, *9*, 806–809.
39. Castro Neto, A. H.; Guinea, F.; Peres, N. M. R.; Novoselov, K. S.; Geim, A. K. The electronic properties of graphene. *Rev. Mod. Phys.* **2009**, *81*, 109–162.
40. Stauber, T.; Peres, N. M. R.; Guinea, F. Electronic Transport in Graphene: A Semiclassical Approach Including Midgap States. *Phys. Rev. B* **2007**, *76*, 205423.
41. Van Tuan, D.; Kotakoski, J.; Louvet, T.; Ortmann, F.; Meyer, J. C.; Roche, S. Scaling Properties of Charge Transport in Polycrystalline Graphene. *Nano Lett.* **2013**, *13*, 1730–1735.
42. Zhang, X. G.; Varga, K.; Pantelides, S. T. Generalized Bloch Theorem for Complex Periodic Potentials: A Powerful Application to Quantum Transport Calculations. *Phys. Rev. B* **2007**, *76*, 035108.
43. Zhang, X. G.; Butler, W. H. Conductivity of Metallic Films and Multilayers. *Phys. Rev. B* **1995**, *51*, 10085–10103.
44. Qin, S. Y.; Kim, T. H.; Zhang, Y. N.; Ouyang, W. J.; Weitering, H. H.; Shih, C. K.; Baddorf, A. P.; Wu, R. Q.; Li, A. P. Correlating Electronic Transport to Atomic Structures in Self-Assembled Quantum Wires. *Nano Lett.* **2012**, *12*, 938–942.
45. Muralt, P.; Pohl, D. W. Scanning Tunneling Potentiometry. *Appl. Phys. Lett.* **1986**, *48*, 514–516.
46. Feenstra, R. M.; Thompson, W. A.; Fein, A. P. Real-Space Observation of Pi-Bond Chains and Surface Disorder on Si(111)2 $\times$ 1. *Phys. Rev. Lett.* **1986**, *56*, 608–611.
47. Fein, A. P.; Kirtley, J. R.; Feenstra, R. M. Scanning Tunneling Microscope for Low-Temperature, High Magnetic-Field, and Spatially Resolved Spectroscopy. *Rev. Sci. Instrum.* **1987**, *58*, 1806–1810.